The Analysis and Calculation of Power Angle Dynamics in Grid Forming Converter Under Large Disturbances Based on KBM Asymptotic Method

Jintao Lei, *Graduate Student Member, IEEE*, Xin Xiang, *Member, IEEE*, Wuhua Li, *Member, IEEE*, and Xiangning He, *Fellow, IEEE*

***Abstract*—Grid forming (GFM) control strategy has been increasingly used in grid-connected converters to regulate system frequency and mimic the inertia of synchronous generator. However, the description of its power angle dynamics under large disturbances is still lacking up to date, which may pose great challenges to stable operation and economic configuration of grid-connected converters in the future power system. To overcome the aforementioned obstacle, a Krylov–Bogoliubov–Mitropolsky (KBM) asymptotic method with the perturbation theory is presented first in this article to derive an analytical solution for power angle trajectory under large disturbances. Considering that the antiderivative problem is usually unsolvable due to the complicated perturbation function, a tailored integral method is further proposed to address this problem and simplify the final result, which facilitates the KBM asymptotic method to the analysis and calculation of power angle trajectory. As a result, an explicit and accurate time-domain expression is obtained, and it reveals the quantitative relationships between control parameters and dynamic characteristics, which may provide a good potential for system transient stability analysis and GFM converter design. In the end, the effectiveness and accuracy of the proposed method are verified by both simulations and control-hardware-in-loop experiments.**

***Index Terms*—Analytical calculation, explicit solution, grid forming converter, Krylov–Bogoliubov–Mitropolsky (KBM) asymptotic method, power angle dynamics.**

I. Introduction

POWER electronic converter (PEC), the main interface between renewable energy sources (RES) and power grid, is becoming an important part of power system with the explosive growth of RES [1], [2], [3], [4], [5]. However, the massive penetration of power electronic interfaced power sources currently reduces the stiffness of grid rapidly because most of PECs are controlled as current sources, and thus, lack of frequency regulation capability [6], [7], which in turn also threatens the stability of PECs. Grid forming (GFM) control, which has the capability to mimic the internal mechanisms and external behaviors of the synchronous generator (SG), is further proposed and regarded as a preferred solution for weak grid [8]. Nonetheless, due to the limited current capacity of PECs, current limiting control is usually triggered under large disturbances such as grid faults, which may still result in a series of system transient instability in weak grid [9], [10], [11], [12]. Thanks to the emerging development of transient overcurrent capacity enhancement in recent years in terms of device packaging [13], [14], [15], modulation [16], [17], [18], and control [19], [20], [21], PECs has begun to have the capability to withstand some large currents in a short-term timescale, such as 3-p.u. current in 3 s [14], which may enable the GFM control under large disturbances within the system transient process. In addition, virtual impedance-based current limiting methods have also been proposed recently to maintain the grid forming capability of the GFM converter under grid fault situations [22], which has similar characteristics to pure GFM control except for the value of equivalent grid impedance. However, the clear description of GFM control transient process is relatively rare and needs to be explored and investigated.

Although GFM control is partially inherited from SG, its transient characteristics are quite different from traditional SG due to the flexible control and fast response [23], [24]. Among these transient characteristics, power angle dynamics, which describes the synchronization process between grid-connected equipment and power grid, is the essential feature of ac power system. A necessary condition for system operation is that all the grid-connected equipment remain in synchronism [25], [26], and so, the power angle dynamics is the fundamental characteristics for grid-connected converters and plays a significant role in system operation. The unknown relationships between control parameters and power angle dynamics of GFM control would pose great challenges to transient stability analysis of system and optimization design of the GFM converter in the future power system with high penetration of RES. Therefore, an intuitive and accurate description of power angle dynamics is urgently required to address this emerging problem.

There are several tools that are usually used for the transient characteristic analysis of grid-connected converter: simulation, power-angle ($P-\delta$) curve, and phase portrait. Simulation

Manuscript received 20 May 2022; revised 7 August 2022; accepted 1 September 2022. Date of publication 14 September 2022; date of current version 18 November 2022. This work was supported in part by the National Key Research and Development Program of China under Grant 2022YFE0101900, and in part by the National Natural Science Foundation of China under Grant 52107214 and Grant 51925702. Recommended for publication by Associate Editor M. Molinas. *(Corresponding author: Xin Xiang.)*

The authors are with the College of Electrical Engineering, Zhejiang University, Hangzhou 310027, China (e-mail: leijintao@zju.edu.cn; xiangxin@zju.edu.cn; woohualee@zju.edu.cn; hxn@zju.edu.cn).

Color versions of one or more figures in this article are available at https://doi.org/10.1109/TPEL.2022.3206497.

Digital Object Identifier 10.1109/TPEL.2022.3206497

method could acquire precise results [27], [28], [29], but the physical insight of power angle dynamics and the explicit relationships between control parameters and transient trajectory are unattainable. The power-angle curve with equal area criterion (EAC) shows its good advantages in power angle dynamic analysis for traditional power system and is introduced to analyze the transient behaviors of GFM control due to its simple form and clear physical meaning [10], [12], [30]. However, the speed governor control in GFM control is deeply coupled to rotor motion [31], resulting in large damp coefficient and affecting the behavior of power angle seriously under large disturbances. The work done by damping torque cannot be reflected in the area of segments between the power angle curve and reference power curve in the power angle diagram, and thus, the effect of damping term is impossible to be taken into account, making it unsuitable for the analysis of large damping system. The phase portrait, a commonly used graphical method for nonlinear system analysis, shows the relationship between power angle and its derivative intuitively [32], [33], [34]. However, its basic equations are still implicit, and the transient trajectory depends deeply on simulation or numerical iteration, making it difficult to obtain explicit quantitative relationships.

Therefore, new tools need to be introduced. The analytical calculation methods based on parameter perturbation theory in nonlinear mechanics, like Krylov–Bogoliubov (K-B) averaging method [35] and first-order multiscale method [36], have been creatively introduced to solve the phase-locked loop (PLL) dynamics in grid following converter, and the transient process is described as an explicit expression. However, these first-order methods would lead to over averaging of the complicated perturbation function in PECs, resulting in a reduction of accuracy in the case of large disturbances. Moreover, the power angle dynamic behavior of GFM control, which is influenced by large damping coefficient and totally different from that of PLL, has not been considered so far.

To the best knowledge of authors, the intuitive description of GFM power angle dynamics is unsolved using the analysis methods previously. In this article, the Krylov–Bogoliubov–Mitropolsky (KBM) asymptotic method, which is a combination of the first-order averaging method and parameter perturbation theory, is adopted to address this challenge. It is first proposed by Krylov in the study of nonlinear mechanics in 1947 [37] and strictly proved by Bogoliubov in 1961 [38], and subsequently, extended to nonstationary vibrations by Mitropolsky in 1965 [39]. This method has shown great advantages in solving high-order transient solution of the dissipation system, and thus, it can obtain quite accurate expressions for amplitude differential and phase differential of the power angle trajectory. However, their original expressions are complicated series summations due to the complex perturbation function, making the antiderivative difficult to solve. To overcome this difficulty, a tailored integral method is further proposed in this article with the consideration of the characteristics of power angle, which not only solves the indefinite integral problem, but also greatly simplifies the calculation results. As a result, the power angle dynamics of GFM control can be approximated by a time-domain explicit function, and hence, the impact of control parameters and grid conditions on it can be revealed quantitatively, which

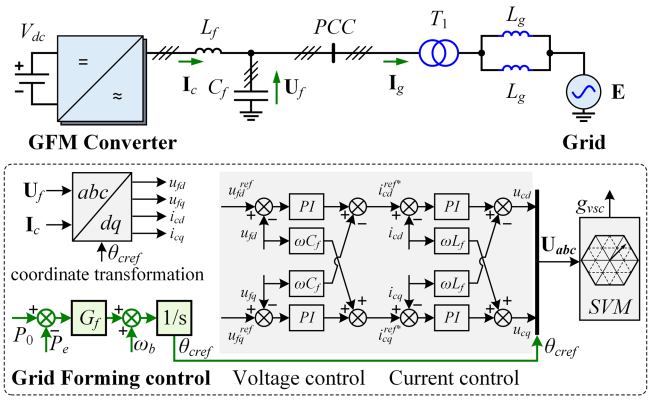

Fig. 1. Circuit and control structure of the GFM converter.

may provide good and effective guidance for system transient stability analysis and GFM converter design. The rest of this article is organized as follows. Section II first establishes the typical model of the grid-connected GFM converter and symmetrical grid fault. In Section III, the power angle dynamics of GFM control is analyzed and calculated in detail with the KBM asymptotic method, and a tailored integral method is also presented in this section. Sections IV and V demonstrate the simulation and experimental validation, respectively. Finally, Section VI concludes this article.

II. Modeling of the Grid-Connected System

A typical grid-connected model of the GFM converter and an equivalent circuit model of symmetrical grid fault are illustrated in this section. Moreover, swing equation is adopted to describe the power angle dynamics of GFM control, which is further written in a standard form.

A. System Descriptions

Fig. 1 shows the single line diagram of a single machine infinite-bus system, where the GFM converter feeds power to the grid through transformer T_1 and two paralleled transmission lines. The impedance of each transmission line is considered as a pure inductance L_g and the grid is simplified to a voltage source presented by vector $\mathbf{E}$ with fundamental frequency ω_b. A typical *LC* filter composed of inductor L_f and capacitor C_f is adopted in the GFM converter. In terms of control, the converter is regulated by an outer grid forming power control loop with inertia simulation, and the inner loop includes both alternating-voltage control (AVC) and current control. The inner AVC loop tracks the voltage reference and maintains the voltage magnitude at the point of common coupling (PCC) constant. In general, the control bandwidth of outer loop is much less than that of inner loop, and thus, the transient response of the inner voltage loop is generally ignored when analyzing power angle dynamic process. Then, the amplitude of the capacitor voltage U_f can be approximated as voltage reference U_{ref}.

The typical inertial GFM control schemes in literatures, including virtual synchronous generator (VSG) control and droop control with a low-pass filter (LPF), are shown in Fig. 2. It has been proved in [40] that these two typical schemes are identical,

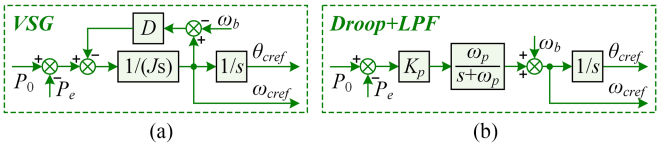

Fig. 2. Typical inertial GFM control schemes. (a) VSG control. (b) Droop control with an LPF.

and their equivalence can be expressed as

$$K_p = \frac{1}{D_p}, \qquad \omega_p = \frac{D_p}{J} \tag{1}$$

where J is the virtual inertia, which slows down the change of reference frequency ω_{cref}, and D_p is the damping coefficient in VSG control. In droop control, K_p is the droop coefficient and ω_p is the cutoff frequency of the LPF applied to simulate the inertia. P_e and P_0 are output active power and its reference, respectively, and the phase θ_{cref} can be seen as an integration of ω_{cref}. In the following analysis, the droop control with an LPF is used as an example. Consequently, the control law of GFM control can be written as

$$\theta_{\text{cref}} = \frac{1}{s}\left[\omega_b + \frac{K_p\omega_p}{s+\omega_p}\left(P_0 - P_e\right)\right]. \tag{2}$$

Defining the initial phase angle of grid voltage **E** as zero, the phase difference between GFM converter and power system, which is known as power angle δ, will be

$$\delta = \frac{1}{s}\frac{K_p\omega_p}{s+\omega_p}\left(P_0 - P_e\right). \tag{3}$$

Considering the circuit structure in Fig. 1, active power P_e from the PCC point can be derived as

$$P_e = \frac{EU_{\text{ref}}}{X_{ge}}\sin\delta \tag{4}$$

where the impedance

$$X_{ge} = X_{T1} + X_g/2 \tag{5}$$

is the equivalent grid impedance under normal operating condition. X_{T1} and X_g are the impedance of transformer T_1 and single transmission line, respectively. Combining (3) and (4), the swing equation of the GFM converter can be described as

$$\delta'' + \omega_p\delta' - K_p\omega_p\left(P_0 - \frac{EU_{\text{ref}}}{X_{ge}}\sin\delta\right) = 0. \tag{6}$$

B. Equivalent Circuit Under Large Disturbances

There are varieties of large disturbances in the power system, like a short or open circuit fault in transmission line, removal of large load or generator, etc. These disturbances usually cause the abrupt change of equivalent impedance X_{ge} or equivalent grid voltage sag, which then result in the transient adjustment of the grid-connected equipment. Among these various disturbances, symmetrical three-phase to ground fault of transmission line is one of the most serious failures and is taken as an example in this article. The actual fault circuit configuration of the grid-connected system in Fig. 2 is shown in Fig. 3(a). X_{gnd} represents the grounding impedance and k is the ratio of the distance from the transformer to short-circuit point and the total length of transmission line, which indicates the severity of

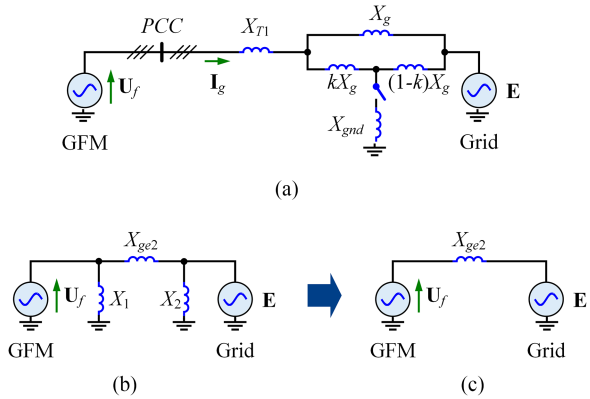

Fig. 3. Fault circuit configuration. (a) Fault circuit. (b) Delta-type equivalent circuit. (c) Simplified equivalent circuit.

faults. Applying delta-wye conversion formulas, the equivalent fault circuit and its simplified circuit model can be obtained as Fig. 3(b) and (c). X_1 and X_2 are the equivalent local impedance in parallel with the GFM converter and power grid, respectively. Since the grid voltage is kept at the equivalent voltage source E and the PCC voltage of GFM converter is also maintained at the voltage reference U_{ref} through inner alternating-voltage control (AVC), the impedances of X_1 and X_2 are, therefore, only related to the reactive power of its corresponding branches and have little effect on E and U_f. Hence, X_1 and X_2 hardly affects the active power transfer between GFM converter and the power grid, and thereby, is negligible when analyzing the active power - angle $(P_e - \delta)$ characteristics. X_{ge2} is the equivalent impedance between GFM converter and utility grid under this fault condition, through which the grid interacts with the GFM converter. The value of

$$X_{ge2} = X_{T1} + X_g + \frac{(1-k)X_{T1} - X_{\text{gnd}}}{k(1-k)X_g + 2X_{\text{gnd}}}X_g \tag{7}$$

mainly relates to fault position k and grounding impedance X_{gnd}, both of which can achieve the same effect. Therefore, for simplicity of analysis, one of them can be set to a fixed value, while the other is variable to change equivalent fault impedance X_{ge2} in simulations or experiments. Based on the aforementioned analysis, three-phase symmetrical grounding fault of transmission line can be regarded as a sudden change of equivalent grid impedance from X_{ge} to X_{ge2}, and the value of X_{ge2} reflects fault severity. The swing equation of the GFM converter under grid fault condition will then be (8). Its new equilibrium point δ_e after grid fault can be calculated by assuming δ' and δ'' are 0, and is shown as (9).

$$\delta'' + \omega_p\delta' - K_p\omega_p\left(P_0 - \frac{EU_{\text{ref}}}{X_{ge2}}\sin\delta\right) = 0 \tag{8}$$

$$\delta_e = \arcsin\left[P_0X_{ge2}/\left(EU_{\text{ref}}\right)\right]. \tag{9}$$

In addition, there will be no abrupt change in power angle due to virtual inertia and the initial change rate of angle is considered to be 0 in this case. Hence, the initial conditions can be written as

$$\delta_0 = \arcsin\left[P_0X_{ge}/\left(EU_{\text{ref}}\right)\right] \quad \text{and} \quad \delta_0' = 0. \tag{10}$$

C. Standard Form Swing Equation

To apply perturbation method to solve the dynamic trajectory of power angle, the swing equation in (8) needs to be decomposed into solvable and perturbative parts. The choice of different solvable problems may influence the complexity and accuracy of calculation. For the second-order vibration system, simple harmonic motion (SHM) is usually chosen as the solvable problem. Moreover, considering the equilibrium point and defining $\gamma = \delta - \delta_e$, this quasi-linear autonomous system can be written in a standard form as

$$\gamma'' + \omega_o^2 \gamma = \varepsilon f(\gamma, \gamma'). \tag{11}$$

ε is set to the cutoff frequency ω_p, which is generally a small parameter in GFM control. ω_o shown as (12) is the free oscillation frequency, and $f(\gamma, \gamma')$ is the perturbation function. Applying the Taylor expansion to trigonometric functions, this perturbation function can be written in a Taylor series form as (13).

$$\omega_o = \sqrt{K_p \omega_p P_0 / \tan \delta_e} \tag{12}$$

$$\begin{aligned} f(\gamma, \gamma') = & -\gamma' + \sum_{n=1}^{\infty} \frac{\omega_o^2}{\omega_p} \frac{(-1)^{n+1}}{(2n+1)!} \gamma^{2n+1} \\ & + \sum_{n=1}^{\infty} \frac{\omega_o^2}{\omega_p} \tan \delta_e \frac{(-1)^{n+1}}{(2n)!} \gamma^{2n}. \end{aligned} \tag{13}$$

At the same time, the initial conditions in (10) can be rewritten as

$$\gamma_0 = \delta_0 - \delta_e \quad \text{and} \quad \gamma_0' = 0. \tag{14}$$

III. Asymptotic Solutions of Power Angle Dynamics

The KBM asymptotic method can solve a high-order solution for the sake of accuracy and show great advantages in solving the dynamic process of dissipative movement. In this section, its second-order form is taken as an example to calculate the power angle characteristic for simplicity. Moreover, a tailored integral method is presented to enable the KBM asymptotic method to solve swing equation with complicated perturbation function and simplify calculation results.

A. Principle of the KBM 2nd Asymptotic Method

First, set the perturbance parameter ε to be zero and the unperturbed motion will be an SHM. The solution of the solvable problem is in the form of trigonometric function and shown as follows:

$$\gamma = a \cos(\omega_o t + \theta). \tag{15}$$

Based on the idea of parameter perturbation, the approximate solution is then set to be power series of ε and so are a' and φ'.

$$\begin{aligned} \gamma &= a \cos \varphi + \varepsilon \gamma_1(a, \varphi) + \varepsilon^2 \gamma_2(a, \varphi) + \cdots \\ a' &= \varepsilon A_1(a) + \varepsilon^2 A_2(a) + \varepsilon^3 A_3(a) + \cdots \\ \varphi' &= \omega_0 + \varepsilon B_1(a) + \varepsilon^2 B_2(a) + \varepsilon^3 B_3(a) + \cdots. \end{aligned} \tag{16}$$

For simplicity, the second-order solution is taken as an example to introduce the solution process of the KBM asymptotic method. The high-order approximate solution, which is more accurate, can be calculated in the same way theoretically if necessary. For the second-order solution, (16) then can be simplified as

$$\begin{aligned} \gamma &= a \cos \varphi + \varepsilon \gamma_1(a, \varphi) + \varepsilon^2 \gamma_2(a, \varphi) + O\left(\varepsilon^3\right) \\ a' &= \varepsilon A_1(a) + \varepsilon^2 A_2(a) + O\left(\varepsilon^3\right) \\ \varphi' &= \omega_o + \varepsilon B_1(a) + \varepsilon^2 B_2(a) + O\left(\varepsilon^3\right). \end{aligned} \tag{17}$$

Based on (17), the second derivatives of a and φ with respect to t, and the products of these first derivatives can be further deduced. The expressions of a'', φ'', $(a')^2$, $a'\varphi'$, and $(\varphi')^2$ can be written as

$$\begin{aligned} a'' &= \varepsilon \frac{dA_1}{da} a' + O\left(\varepsilon^3\right) = \varepsilon^2 A_1 \frac{dA_1}{da} + O\left(\varepsilon^3\right) \\ \varphi'' &= \varepsilon \frac{dB_1}{da} a' + O\left(\varepsilon^3\right) = \varepsilon^2 A_1 \frac{dB_1}{da} + O\left(\varepsilon^3\right) \\ (a')^2 &= A_1^2 \varepsilon^2 + O\left(\varepsilon^3\right) \\ a'\varphi' &= \omega_0 A_1 \varepsilon + \left(A_1 B_1 + \omega_0 A_2\right) \varepsilon^2 + O\left(\varepsilon^3\right) \\ (\varphi')^2 &= \omega_0^2 + 2\omega_0 B_1 \varepsilon + \left(B_1^2 + 2\omega_0 B_2\right) \varepsilon^2 + O\left(\varepsilon^3\right). \end{aligned} \tag{18}$$

Moreover, the specific expressions of γ' and γ'' are also required when applying the second-order asymptotic method. Taking the first and second derivatives of γ with respect to t, their expressions are shown as follows:

$$\gamma' = a' \left[\cos \varphi + \sum_{i=1}^{2} \varepsilon^i \frac{\partial \gamma_i}{\partial a}\right] - \varphi' \left[a \sin \varphi - \sum_{i=1}^{2} \varepsilon^i \frac{\partial \gamma_i}{\partial \varphi}\right] \tag{19}$$

$$\begin{aligned} \gamma'' = & a'' \cos \varphi - \varphi'' a \sin \varphi - 2a'\varphi' \sin \varphi - [\varphi']^2 a \cos \varphi \\ & + a'' \sum_{i=1}^{2} \varepsilon^i \frac{\partial \gamma_i}{\partial a} + \varphi'' \sum_{i=1}^{2} \varepsilon^i \frac{\partial \gamma_i}{\partial \varphi} + [a']^2 \sum_{i=1}^{2} \varepsilon^i \frac{\partial^2 \gamma_i}{\partial a^2} \\ & + 2a'\varphi' \sum_{i=1}^{2} \varepsilon^i \frac{\partial^2 \gamma_i}{\partial a \partial \varphi} + [\varphi']^2 \sum_{i=1}^{2} \varepsilon^i \frac{\partial^2 \gamma_i}{\partial \varphi^2}. \end{aligned} \tag{20}$$

Considering these derivatives in (18), γ'' can be written in the form of power series of ε. Then, γ and γ'' are further substituted into the left side of the perturbed equation (11) and rearranged in the order of ε. As a result, the left side of the swing equation can be written as

$$\begin{aligned} & \gamma'' + \omega_o^2 \gamma \\ & = \varepsilon \left[-2\omega_o A_1 \sin \varphi - 2\omega_0 a B_1 \cos \varphi + \omega_o^2 \left(\frac{\partial^2 \gamma_1}{\partial \varphi^2} + \gamma_1\right)\right] \\ & \quad + \varepsilon^2 \begin{bmatrix} A_1 \frac{dA_1}{da} \cos \varphi - a B_1^2 \cos \varphi - 2\omega_o a B_2 \cos \varphi \\ -a A_1 \frac{dB_1}{da} \sin \varphi - 2A_1 B_1 \sin \varphi - 2\omega_o A_2 \sin \varphi \\ +2\omega_o B_1 \frac{\partial^2 \gamma_1}{\partial \varphi^2} + 2\omega_o A_1 \frac{\partial^2 \gamma_1}{\partial a \partial \varphi} + \omega_o^2 \left(\frac{\partial^2 \gamma_2}{\partial \varphi^2} + \gamma_2\right) \end{bmatrix} \\ & \quad + O\left(\varepsilon^3\right). \end{aligned} \tag{21}$$

Similarly, substituting (17) and (19) into the right side of the perturbed equation (11), and expanding it into a power series of

ε, there will be

$$\begin{aligned}\varepsilon f(\gamma,\gamma') &= \varepsilon f(a\cos\varphi, -a\omega_o\sin\varphi)\\ &+ \varepsilon^2\left[\gamma_1\frac{\partial f}{\partial\gamma} + \left(A_1\cos\varphi - aB_1\sin\varphi + \omega_o\frac{\partial\gamma_1}{\partial\varphi}\right)\frac{\partial f}{\partial\gamma'}\right]\\ &+ O\left(\varepsilon^3\right). \end{aligned} \tag{22}$$

Then, compare the coefficients of the corresponding powers of ε as

$$\begin{aligned}\varepsilon &: \omega_o^2\frac{\partial^2\gamma_1}{\partial\varphi^2} + \omega_o^2\gamma_1 = f_0(a,\varphi)\\ &\qquad +2\omega_o\left(A_1\sin\varphi + aB_1\cos\varphi\right)\\ \varepsilon^2 &: \omega_o^2\frac{\partial^2\gamma_2}{\partial\varphi^2} + \omega_o^2\gamma_2 = f_1(a,\varphi)\\ &\qquad +2\omega_0\left(A_2\sin\varphi + aB_2\cos\varphi\right)\end{aligned} \tag{23}$$

in which

$$\begin{aligned}f_0(a,\varphi) &= f(a\cos\varphi, -a\omega_0\sin\varphi)\\ f_1(a,\varphi) &= \left[aA_1\frac{dB_1}{da} + 2A_1B_1 - aB_1\frac{\partial f}{\partial\gamma'}\right]\sin\varphi\\ &+ \left[aB_1^2 - A_1\frac{dA_1}{da} + A_1\frac{\partial f}{\partial\gamma'}\right]\cos\varphi + \gamma_1\frac{\partial f}{\partial\gamma}\\ &+ \omega_o\frac{\partial\gamma_1}{\partial\varphi}\frac{\partial f}{\partial\gamma'} - 2\omega_oA_1\frac{\partial^2\gamma_1}{\partial a\partial\varphi} - 2\omega_oB_1\frac{\partial^2\gamma_1}{\partial\varphi^2}.\end{aligned} \tag{24}$$

To determine the unknown variables A_1, B_1, and γ_1, $f_0(a,\varphi)$ is then expanded to Fourier series as

$$f_0(a,\varphi) = g_0(a) + \sum_{n=1}^{\infty}\left[g_n(a)\cos n\varphi + h_n(a)\sin n\varphi\right]. \tag{25}$$

Considering the elimination of secular term, the coefficients of $\sin\varphi$ and $\cos\varphi$ on the right-hand side of the first equation in (23) is set to be 0. As a result, A_1 and B_1 become

$$\begin{aligned}A_1 &= \frac{-h_1(a)}{2\omega_o}\\ &= \frac{-1}{2\pi\omega_o}\int_0^{2\pi} f(a\cos\varphi, -a\omega_o\sin\varphi)\sin\varphi d\varphi\\ B_1 &= \frac{-g_1(a)}{2a\omega_o}\\ &= \frac{-1}{2\pi a\omega_o}\int_0^{2\pi} f(a\cos\varphi, -a\omega_o\sin\varphi)\cos\varphi d\varphi.\end{aligned} \tag{26}$$

Then, γ_1 can be calculated as

$$\gamma_1 = \frac{g_0(a)}{\omega_o^2} + \sum_{n=2}^{\infty}\frac{g_n(a)\cos n\varphi + h_n(a)\sin n\varphi}{\omega_o^2\left(1-n^2\right)}. \tag{27}$$

With the expressions of A_1, B_1, and γ_1, $f_1(a,\varphi)$ can also be expanded to Fourier series as

$$f_1(a,\varphi) = g_0^1(a) + \sum_{n=1}^{\infty}\left[g_n^1(a)\cos n\varphi + h_n^1(a)\sin n\varphi\right]. \tag{28}$$

Then, A_2, B_2, and γ_2 can be solved by the same method and the solutions are

$$\begin{aligned}A_2 &= -\frac{h_1^1(a)}{2\omega_0} = -\frac{1}{2\pi\omega_0}\int_0^{2\pi} f_1(a,\varphi)\sin\varphi d\varphi\\ B_2 &= -\frac{g_1^1(a)}{2a\omega_0} = -\frac{1}{2\pi a\omega_0}\int_0^{2\pi} f_1(a,\varphi)\cos\varphi d\varphi\\ \gamma_2 &= \frac{g_0^1(a)}{\omega_0^2} + \sum_{n=2}^{\infty}\frac{g_n^1(a)\cos n\varphi + h_n^1(a)\sin n\varphi}{\omega_0^2\left(1-n^2\right)}.\end{aligned} \tag{29}$$

Then, combining (17), (26), (27), and (29), a and φ can be obtained by integrating with respect to time t, and their initial values are also determined by boundary conditions in (14).

B. Second-Order Asymptotic Solution of Power Angle

Based on the SHM solution in (15), high power of γ_0 can be easily expanded by the trigonometric function transformation as

$$\gamma_0^m = \sum_{n=0}^{m} C_{(m)n}a^m\cos n\varphi \tag{30}$$

where $C_{(m)n}$ is the nth harmonic coefficient of mth power of γ_0 and can be calculated through (31) due to the properties of the trigonometric function.

$$\begin{aligned}C_{(m)n} &= \frac{C_m^{\frac{m-n}{2}}}{2^{m-1}} : n\neq 0\wedge(m-n) = 2k(k=0,1,2\ldots)\\ C_{(m)n} &= \frac{C_m^{\frac{m-n}{2}}}{2^m} : n = 0\wedge(m-n) = 2k(k=0,1,2\ldots)\\ C_{(m)n} &= 0 : \text{others}\end{aligned} \tag{31}$$

where C_m^n is the combination value of n objects selected from a group of m members, and $C_{(m)n}$ is zero if the parity of m and n are different. In the case of the perturbation function (13), the Fourier coefficients of $f_0(a,\varphi)$ can be calculated by using the expansion in (30) and shown as

$$\begin{aligned}g_n(a) &= \omega_o^2N_n/\omega_p + K_pP_0M_n\\ h_n(a) &= -a\omega_o : n = 1\\ h_n(a) &= 0 : n\geq 2\end{aligned} \tag{32}$$

where M_n and N_n are the series summations caused by the perturbation function $f(\gamma,\gamma')$, which are

$$\begin{aligned}M_n &= \sum_{i=1}^{\infty}\frac{C_{(2i)n}a^{2i}}{(-1)^{i+1}(2i)!}\\ N_n &= \sum_{i=1}^{\infty}\frac{C_{(2i+1)n}a^{2i+1}}{(-1)^{i+1}(2i+1)!}.\end{aligned} \tag{33}$$

Considering the value of $C_{(m)n}$, M_n is zero when n is odd and N_n is zero when n is even. On the basis of (33), their products, M_mM_n, M_mN_n, and N_mN_n, can be further derived as double

summation formulas as

$$M_m M_n = \sum_{i=2}^{\infty}\sum_{j=1}^{i-1} \frac{C_{(2j)m}C_{(2i-2j)n}a^{2i}}{(-1)^i(2j)!(2i-2j)!}$$

$$M_m N_n = \sum_{i=2}^{\infty}\sum_{j=1}^{i-1} \frac{C_{(2j)m}C_{(2i-2j+1)n}a^{2i+1}}{(-1)^i(2j)!(2i-2j+1)!}$$

$$N_m N_n = \sum_{i=2}^{\infty}\sum_{j=1}^{i-1} \frac{C_{(2j+1)m}C_{(2i-2j+1)n}a^{2i+2}}{(-1)^i(2j+1)!(2i-2j+1)!}. \quad (34)$$

Substituting the Fourier coefficients in (32) to (26) and (27), A_1, B_1, and γ_1 can be solved as

$$A_1 = -a/2, \quad B_1 = -\omega_o N_1/(2a\omega_p)$$

$$\gamma_1 = \frac{\tan\delta_e M_0}{\omega_p} + \sum_{n=2}^{\infty}\left(\frac{N_n}{\omega_p} + \frac{\tan\delta_e M_n}{\omega_p}\right)\frac{\cos n\varphi}{1-n^2}. \quad (35)$$

Combining (33) and (35), the derivatives of A_1 and B_1 with respect to a can be deduced as

$$\frac{dA_1}{da} = -\frac{1}{2}, \quad \frac{dB_1}{da} = \sum_{i=1}^{\infty}\frac{i\omega_o C_{(2i+1)1}a^{2i-1}}{(-1)^i\omega_p(2i+1)!}. \quad (36)$$

Further, the first and second partial derivatives of γ_1 with respect to φ or a are derived as (37).

$$\frac{\partial\gamma_1}{\partial\varphi} = \sum_{n=2}^{\infty}\left[-\left(\frac{N_n}{\omega_p} + \frac{\tan\delta_e M_n}{\omega_p}\right)\frac{n\sin n\varphi}{1-n^2}\right]$$

$$\frac{\partial^2\gamma_1}{\partial\varphi^2} = \sum_{n=2}^{\infty}\left[-\left(\frac{N_n}{\omega_p} + \frac{\tan\delta_e M_n}{\omega_p}\right)\frac{n^2\cos n\varphi}{1-n^2}\right]$$

$$\frac{\partial^2\gamma_1}{\partial a\partial\varphi} = \sum_{n=2}^{\infty}\sum_{i=1}^{\infty}\left[\frac{1}{\omega_p}\frac{C_{(2i+1)n}a^{2i}}{(-1)^i(2i)!}\frac{n\sin n\varphi}{1-n^2}\right] + \sum_{n=2}^{\infty}\sum_{i=1}^{\infty}\left[\frac{\tan\delta_e}{\omega_p}\frac{C_{(2i)n}a^{2i-1}}{(-1)^i(2i-1)!}\frac{n\sin n\varphi}{1-n^2)}\right]. \quad (37)$$

To solve $f_1(a,\varphi)$, the partial derivatives of $f(\gamma,\gamma')$ to γ and γ' are also required according to (24). It can be derived from the Taylor expansion of perturbation function in (13) and shown as

$$\frac{\partial f}{\partial\gamma'} = -1$$

$$\frac{\partial f}{\partial\gamma} = \sum_{n=0}^{\infty}\frac{\omega_o^2}{\omega_p}\left[M_n - \tan\delta_e\left(N_n - C_{(1)n}a\right)\right]\cos n\varphi. \quad (38)$$

Substituting the aforementioned equations into $f_1(a,\varphi)$ and rearranging it in the form of trigonometric function summations, the coefficients $h_n^1(a)$ of $\sin n\varphi$ and $g_n^1(a)$ of $\cos n\varphi$ will be obtained by comparing it with Fourier expansion in (28). Considering the fundamental frequency component, their coefficients, $h_1^1(a)$ and $g_1^1(a)$, are

$$h_1^1(a) = -\frac{\omega_o}{\omega_p}\sum_{i=1}^{\infty}\frac{iC_{(2i+1)1}a^{2i+1}}{2(-1)^i(2i+1)!}$$

$$g_1^1(a) = \frac{a}{4} + \frac{\omega_o^2}{\omega_p^2}\sum_{m=2}^{\infty}\frac{N_m\left(M_{m+1}+M_{m-1}\right)}{2\left(1-m^2\right)} - \frac{\omega_o^2\tan^2\delta_e}{\omega_p^2}\sum_{m=2}^{\infty}\frac{M_m\left(N_{m+1}+N_{m-1}\right)}{2\left(1-m^2\right)} + \frac{\omega_o^2 N_1^2}{4a\omega_p^2} + \frac{\omega_o^2\tan^2\delta_e}{\omega_p^2}\left[aM_0 - M_0N_1 - \frac{aM_2}{6}\right]. \quad (39)$$

According to (39), the quadratic coefficients A_2 and B_2 can be solved by substituting the detailed expressions of $h_1^1(a)$ and $g_1^1(a)$ into (29) though it is complicated. The expressions in form of sums are shown as

$$A_2 = \frac{1}{2\omega_p}\sum_{i=1}^{\infty}\frac{iC_{(2i+1)1}a^{2i+1}}{2(-1)^i(2i+1)!}$$

$$B_2 = -\frac{1}{8\omega_o} - \frac{\omega_o}{\omega_p^2}\sum_{m=2}^{\infty}\frac{N_m\left(M_{m+1}+M_{m-1}\right)}{4a\left(1-m^2\right)} + \frac{\omega_o\tan^2\delta_e}{2\omega_p^2}\sum_{m=2}^{\infty}\frac{M_m\left(N_{m+1}+N_{m-1}\right)}{2a\left(1-m^2\right)} - \frac{\omega_o N_1^2}{8a^2\omega_p^2} - \frac{\omega_o\tan^2\delta_e}{2\omega_p^2}\left[M_0 - \frac{M_0N_1}{a} - \frac{M_2}{6}\right]. \quad (40)$$

Combining A_1, B_1, A_2, and B_2, the second-order solutions of amplitude differential a' and phase differential φ' in (17) can be written in detail as

$$a' = -\frac{\omega_p a}{2} + \frac{\omega_p}{2}\sum_{m=1}^{\infty}\frac{(-1)^m mC_{(2m+1)1}a^{2m+1}}{2(2m+1)!}$$

$$\varphi' = \omega_o - \omega_o\frac{N_1}{2a} - \omega_o\sum_{m=2}^{\infty}\frac{N_m\left(M_{m+1}+M_{m-1}\right)}{4a\left(1-m^2\right)} - \frac{\omega_p^2}{8\omega_o} + \frac{\omega_o\tan^2\delta_e}{2}\sum_{m=2}^{\infty}\frac{M_m\left(N_{m+1}+N_{m-1}\right)}{2a\left(1-m^2\right)} - \omega_o\frac{N_1^2}{8a^2} - \frac{\omega_o\tan^2\delta_e}{2}\left[M_0 - \frac{M_0N_1}{a} - \frac{M_2}{6}\right]. \quad (41)$$

Similarly, the nth Fourier coefficients of $f_1(a,\varphi)$ and γ_2 thus can be calculated in the same way, which contains multilayered series summations and is extremely complicated. Moreover, solving the trajectory of power angle requires the antiderivative of (41). However, due to the complicated series summation form of a' and φ' in (41), it is usually hard to solve the antiderivative. Therefore, more modifications should be made for practical purposes.

C. Tailored Integral Method

Considering the characteristic of power angle, some simplifications are made as follows. First, it can be known from (17) that a' and φ' in (41) are obtained by eliminating small quantities above order ε^3. This approximation will result in errors of order $\varepsilon^3 t$ in both a and φ. In general, ω_p in GFM control is in the range of a few tenths of a Hertz to a few Hertz. Hence, the per-unit value of ε is quite small and the calculation time t in power angle dynamics is usually enough to be several times of $1/\varepsilon$. Hence, the error of a and φ within this time will be ε^2, making it no sense to keep $\varepsilon^2\gamma_2$ in the quadratic approximation result.

Ignoring $\varepsilon^2\gamma_2$, the quadratic approximation result of γ can be written as

$$\gamma = a\cos\varphi + \varepsilon\gamma_1(a,\varphi). \tag{42}$$

Furthermore, the power angle range is within $[0,\pi]$, and therefore, its oscillation amplitude a after grid fault will be smaller than $\pi/2$ or even less than 1 rad for typical static power angle δ_0. At the same time, these coefficients of high powers of a in (41) are usually small enough to be ignored. Considering the main items, the amplitude differential a' can be reduced to

$$a' = -\frac{\omega_p a}{2} - \frac{\omega_p a^3}{32}. \tag{43}$$

Rearranging φ' into the sum of $a^m a'$ and considering the main items, the phase differential φ' can be reduced to

$$\varphi' = \omega_o\left[1 - \frac{\omega_p^2}{8\omega_o^2} + \frac{2}{\omega_p}\left(\frac{1}{16} + \frac{5\tan^2\delta_e}{48}\right)aa'\right]. \tag{44}$$

As seen from (43) and (44), the attenuation rate of amplitude mainly determined by ω_p, while the oscillation frequency φ' is also related to the free oscillation frequency ω_o and the tangent value of the equilibrium position angle $\tan\delta_e$. Moreover, the value of these omitted items in the process of customization increases with the increase of $\tan\delta_e$ and A_0, which results in increased error of the calculation result. On top of that, the amplitude a and phase φ can be obtained by integrating (43) and (44), which are shown as

$$\begin{aligned} a &= \frac{4A_0 e^{-\frac{\omega_p t}{2}}}{\sqrt{16 + A_0^2 - A_0^2 e^{-\omega_p t}}} \\ \varphi &= \varphi_0 + \omega_o\left(1 - \frac{\omega_p^2}{8\omega_o^2}\right)t + \frac{\omega_o}{\omega_p}\left(\frac{1}{16} + \frac{5\tan^2\delta_e}{48}\right)a^2. \end{aligned} \tag{45}$$

Similarly, γ_1 in (35) can also be reduced to

$$\gamma_1 = \frac{\tan\delta_e}{\omega_p}\left[\frac{a^2}{4} - \frac{a^4}{64} - \left(\frac{a^2}{12} - \frac{a^4}{144}\right)\cos 2\varphi\right]. \tag{46}$$

Substituting (45) and (46) into (42), the quadratic approximation solution can be obtained, and the initial value A_0 and φ_0 can be solved using these boundary conditions in (14). Finally, considering $\gamma = \delta - \delta_e$, the time-domain expression of the power angle δ can be written as

$$\delta = \delta_e + a\cos\varphi + \varepsilon\gamma_1(a,\varphi). \tag{47}$$

D. Effect of Reactive Power Control

Except AVC control, the voltage of the GFM converter at PCC point can also be controlled by reactive power–voltage ($Q-V$) droop control. When considering the $Q-V$ droop characteristic, X_2 in equivalent fault circuit still can be ignored, whereas X_1 needs to be preserved. The Delta-type equivalent circuit in Fig. 3(b) then can be simplified as Fig. 4 and the local impedance X_1 can be written as

$$X_1 = (1+k)X_{T1} + kX_g + \frac{X_{\text{gnd}}(X_g + 2X_{T1})}{(1-k)X_g}. \tag{48}$$

The $Q-V$ droop law and the reactive power transmitted from the PCC point can be written as (49) and (50), respectively, where

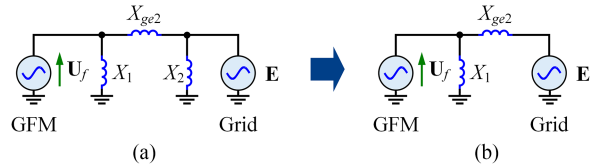

Fig. 4. Simplified equivalent fault circuit considering $Q-V$ droop control. (a) Delta-type equivalent circuit. (b) Simplified equivalent circuit.

Q_e and Q_0 are the reactive power and its reference. K_q is $Q-V$ droop coefficient and U_0 is voltage reference.

$$U_f = U_0 + K_q(Q_0 - Q_e) \tag{49}$$

$$Q_e = \frac{U_f^2}{X_1} + \frac{U_f^2}{X_{ge2}} - \frac{EU_f\cos\delta}{X_{ge2}}. \tag{50}$$

Substituting (50) into (49) and solving the quadratic equation, the voltage at PCC point U_f, thereby, can be solved in an explicit form as (57) in Appendix. Considering the swing equation and setting ε to the cutoff frequency ω_p, its standard form will still be

$$\gamma'' + \omega_{oq}^2\gamma = \varepsilon f_q(\gamma,\gamma'). \tag{51}$$

ω_{oq} is the free oscillation frequency and its detailed expression is shown as (58) in Appendix. The perturbation function $f_q(\gamma,\gamma')$ considering $Q-V$ droop control can be written in Taylor series form as

$$f_q(\gamma,\gamma') = -\gamma' + \sum_{n=2}^{\infty}\frac{K_p P_{\Delta 0}^{(n)}}{n!}\gamma^n \tag{52}$$

where $P_{\Delta 0}^{(n)}$ is the nth derivatives of power difference $P_\Delta(\gamma)$ in Appendix with respect to γ at $\gamma = 0$. Comparing it with the swing equation based on inner AVC control, the main differences lie in free oscillation frequency and perturbance function expansion coefficients. Therefore, the same derivation process in Section III-B and tailored integral method in Section III-C can still be applied to calculate the power angle dynamics with $Q-V$ droop control. After applying the second-order KBM asymptotic calculating method, the amplitude a and phase φ are derived as

$$\begin{aligned} a &= \frac{4A_0 e^{-\frac{\omega_p t}{2}}}{\sqrt{16 + \frac{\omega_p}{\omega_0^2}K_p P_{\Delta 0}^{(3)}\left[A_0^2 - A_0^2 e^{-\omega_p t}\right]}} \\ \varphi &= \varphi_0 + \omega_o\left(1 - \frac{\omega_p^2}{8\omega_o^2}\right)t + \frac{K_p P_{\Delta 0}^{(3)}}{16\omega_o}a^2 + \frac{5\omega_p K_p^2 P_{\Delta 0}^{(2)2}}{48\omega_o^3}a^2. \end{aligned} \tag{53}$$

Similarly, γ_1 can also be written as

$$\begin{aligned} \gamma_1 = &\frac{K_p}{\omega_o^2}\left(\frac{P_{\Delta 0}^{(2)}}{4}a^2 + \frac{P_{\Delta 0}^{(4)}}{64}a^4\right) \\ &- \frac{K_p}{\omega_o^2}\left(\frac{P_{\Delta 0}^{(2)}}{12}a^2 + \frac{P_{\Delta 0}^{(4)}}{144}a^4\right)\cos 2\varphi. \end{aligned} \tag{54}$$

E. Summary and Discussion

Compared with the first-order K-B averaging method, the second-order KBM asymptotic method have added more details in both attenuation term and steady-state term, making the error level reduce from ε to ε^2. The aperiodic component and the double frequency attenuation component are included in the expression of γ_1, and high-order attenuation components are added to the expression of amplitude differential a' and phase differential φ'. In particular, the effect of ω_p on quasi static oscillation frequency is taken into account in the second-order KBM method and the frequency changes from ω_o to $\omega_o - \omega_p^2/(8\omega_o)$. The effect of these additional terms on accuracy improvement is verified in the simulation in Section IV. Moreover, the second-order KBM asymptotic method can also be applied to second-order nonlinear equations with other controls, corresponding to a modified perturbation function. The approximate results considering AVC control in Section III-C and $Q-V$ droop control in Section III-D have shown the same form with different coefficients, which is mainly determined by the derivative of power difference $P_\Delta(\gamma)$ and only influences the perturbation function $f(\gamma, \gamma')$.

Compared with the numerical iteration or simulation method, the explicit analytical expression is able to establish some quantitative relationships between parameters and transient characteristics. Taking the AVC control as an example, the decaying rate of oscillation amplitude a depends more on the cutoff frequency ω_p than damping coefficient D alone. Therefore, if D increases tenfold, the virtual inertia J should also increase tenfold to maintain a similar amplitude attenuation effect. As for oscillation frequency φ', it is closely related to the value of ω_o/ω_p and $\tan\delta_e$. With the increase of ω_o/ω_p, the influence of the nondecaying component decreases and that of the decaying component increases. For a fixed ω_o/ω_p, the value of $\tan\delta_e$ mainly affects the amplitude of attenuation component. Moreover, the effect of $\varepsilon\gamma_1$, which includes the aperiodic component and the double frequency attenuation component, is also determined by $\tan\delta_e$. When the $Q-V$ droop control is considered, the analytical expression can also be used to analyze the dominant term under various parameters and to what extent do different terms influence the transient characteristics. In this manner, the quantitative relationships between the transient trajectories and parameters obtained from the analytical results may provide a good basis for the transient characteristics regulation and control of GFM converters.

IV. Simulation Verification

To validate the accuracy of analytical calculation results using the second-order KBM asymptotic method, the time-domain simulations have been conducted on the system shown in Fig. 1 with the parameters given in Table I as the reference waveform. It is worth noting that the inner alternating-voltage and current control loops are both implemented in simulations, and the analytical calculations using the second-order KBM asymptotic method match well with the simulations, which verifies these assumptions in the derivation process. Meanwhile, the first-order solution using the K–B averaging method is also illustrated in the figure as a comparison.

TABLE I
Control and Circuit Parameters of GFM Converter

Parameters		Descriptions	Values
Grid	E	Grid voltage	380 V (1.0 p.u.)
	ω_b	Grid frequency	314 rad/s (1.0 p.u.)
	L_g	Single line inductance	36.8 mH (0.8 p.u.)
	L_{T1}	Inductance of transformer	5.5 mH (0.12 p.u.)
	L_{gnd}	Grounding inductance	4.6 mH (0.1 p.u.)
	k	Fault distance	0.0 ~ 0.7
GFM	S_n	Rated power	10 kVA (1.0 p.u.)
	L_f	Filter inductance	1.38 mH (0.03 p.u.)
	C_f	Filter capacitance	50 μF (0.23 p.u.)
	U_{ref}	Voltage reference	380 V (1.0 p.u.)
	P_0	Active power reference	9 kW (0.9 p.u.)
	K_p	Droop coefficient	0.02~0.1 p.u.
	ω_p	Cutoff frequency of LPF in GFM control	0.1·2π rad/s ~1.2·2π rad/s

TABLE II
Parameters for Simulation and Experimental Tests

Parameters	k (X_{ge2})	K_p	ω_p
Case I-A	0.7 (0.78 p.u.)	0.04 p.u.	0.2·2π rad/s
Case I-B	0.3 (0.88 p.u.)	0.04 p.u.	0.2·2π rad/s
Case I-C	0.1 (0.94 p.u.)	0.04 p.u.	0.2·2π rad/s
Case I-D	0.0 (1.00 p.u.)	0.04 p.u.	0.2·2π rad/s
Case II-A	0.1 (0.94 p.u.)	0.02 p.u.	0.2·2π rad/s
Case II-B	0.1 (0.94 p.u.)	0.06 p.u.	0.2·2π rad/s
Case II-C	0.1 (0.94 p.u.)	0.10 p.u.	0.2·2π rad/s
Case III-A	0.1 (0.94 p.u.)	0.04 p.u.	1.2·2π rad/s
Case III-B	0.1 (0.94 p.u.)	0.04 p.u.	0.4·2π rad/s
Case III-C	0.1 (0.94 p.u.)	0.04 p.u.	0.1·2π rad/s

Moreover, ten cases with different configurations of the GFM converter and grid have been tested, and their specific parameter configurations are listed in Table II. Case I-C is the base case. On top of that, the fault location k changes in Case I-A, Case I-B, and Case I-D, resulting in a change in equivalent impedance after fault. In Case II-A–Case II-C, the influence of droop coefficient, which is often determined based on the grid code, is considered. According to IEEE P1547 [41] and EN 50438 [42], the droop coefficient K_p in GFM converters should be in the range of $2\% \sim 12\%$, which means that the change of 100% active power corresponds to the change of $2\% \sim 12\%$ grid frequency. Hence, the droop coefficient K_p of GFM control in this article changes from 0.02 p.u. (Case II-A) to 0.10 p.u. (Case II-C), respectively, corresponding to a damping D of 10 to 50 p.u. The influence of the cutoff frequency ω_p, which reflects the inertia constant of GFM control, is also investigated in Case III. In this manner, the damping D in Case III-A is set to 25 p.u., and its inertia constant is 3.3 s. This inertia value is close to the typical value of the

synchronous generator [43], and it could better demonstrate the inherent large damping effect for GFM converters [40].

A. Impact of Fault Severity

Fig. 5 shows both simulation waveforms and analytical calculation results for power angle dynamic responses of the GFM converter with different fault positions. Before fault, 0.9-p.u. active power is transmitted to power grid and its equivalent grid impedance X_{ge} is 0.52 p.u. Under this grid condition, the static transmission power angle can be calculated through (10), which is 0.155π in radians. Once grid fault occurs at $t = 1.0$ s, equivalent impedance changes from X_{ge} to X_{ge2}. The impedance mutation increases with the decrease of fault distance k, indicating more serious grid fault.

In Case I-A, its fault position is 0.7, which is quite far away from the GFM converter, and thus, results in a small equivalent impedance mutation from 0.52 to 0.78 p.u.. In this case, the calculation results of both first-order method and second-order method shown in Fig. 5(a) fit extremely well with the simulation waveform. As the fault distance k decreases, equivalent fault impedance X_{ge2} increases, and hence, fault severity increases. With the increase of X_{ge2}, the results of K-B averaging solution (green dashed line) deviate significantly from the simulation waveform (blue solid line) as seen from Fig. 5(b) to (d). Meanwhile, second-order KBM asymptotic solution (orange dashed line) and the simulated power angle almost remains overlap in Fig. 5(b) and (c). When X_{ge2} increases to 1.00 p.u., $\tan\delta_e$ and oscillation amplitude increase, resulting in the decrease of free oscillation frequency ω_o. Therefore, the value of the perturbance parameter ε becomes closer to ω_o, and the effect of these omitted items in the process of customization is more obvious. Also, the perturbation function is expanded near the equilibrium point in the calculation process, and thus, the error will also increase with the increase of oscillation amplitude in the case of relatively low expansion order. Considering both factors, the error increases with the increase of equivalent impedance X_{ge2}. As shown in Fig. 5(d), the error mainly appears in the oscillation frequency and gradually decreases with the decrease of the oscillation amplitude, which is consistent with theoretical analysis. Nonetheless, the error in amplitude is still small and second-order KBM asymptotic method keeps its advantages in solving large disturbances cases.

B. Impact of Droop Coefficient

In addition to fault severity, the power angle dynamic characteristics will also be affected by the control parameters of GFM control, including droop coefficient K_p and LPF cutoff frequency ω_p. K_p is closely related to the damping of virtual rotor motion and changes its vibration frequency. The damping effect of GFM control decreases with the increase of K_p, resulting in a slower oscillation amplitude decay rate and larger oscillation frequency. Hence, the power angle variation range will be slightly larger, which further increases its nonlinearity. Fig. 6 shows the influence of droop coefficient K_p of GFM control on δ. Parameters and grid conditions are exactly the same as the base case (Case I-C), except K_p. As can be seen, once fault occurs at $t = 1.0$ s, the difference between first-order K-B calculation result and simulation result increases with the increase of K_p from 0.02 p.u. in Case II-A [see Fig. 6(a)] to 0.1 p.u. in Case II-C [see Fig. 6(d)]. Meanwhile, the deviation between second-order KBM calculation results and the simulation results changes more slowly. However, with the increase of K_p, the control bandwidth of the power control loop increases, which enhances its coupling with the inner control loop. Therefore, as K_p increases to 0.1 p.u., there is a slight deviation shown in Fig. 6(d). Nonetheless, the effect is very small in the typical value range of K_p and so is the error, which further validates the accuracy and advantage of the KBM asymptotic method with different droop coefficients.

C. Impact of Cutoff Frequency

The cutoff frequency of the LPF ω_p also shows great impact on the transient characteristic of the GFM converter. As ω_p decreases, the power angle regulation speed is going to slow down, indicating a larger virtual inertia. Therefore, the power angle oscillation will be larger with a small ω_p and more likely to cause instability, which is an inherent problem of VSG-like control. Fig. 7 presents the transient response of power angle with different LPF cutoff frequencies ω_p in GFM control. In Case III-A, ω_p is $1.2{\cdot}2\pi$ rad/s, which is a quite large value. Therefore, it takes a short time to regulate power angle to steady state and results in a small overshoot. As is depicted in Fig. 7(a), both second-order KBM asymptotic solution and first-order K–B averaging solution have small mismatches with the simulation result at the peak of the waveform. The former is mainly due to the coupling of GFM control loop and inner control loop, while the latter is also affected by the calculation error of the method itself. As ω_p decreases to $0.4{\cdot}2\pi$ rad/s in Case III-B, $0.2{\cdot}2\pi$ rad/s in Case I-C and even $0.1{\cdot}2\pi$ rad/s in Case III-C, the power angle oscillation range increases and the nonlinearity of oscillation is increased. Thus, the errors of both methods are likely to increase. As shown in Fig. 7(b) to (d), the error of first-order K-B calculation results keeps increasing significantly. In contrast, the second-order KBM solution could still remain in line with the simulation waveform and even better than Case III-A due to the reduction of loop coupling. As a result, the effectiveness and advantages of second-order KBM asymptotic method are validated under various virtual inertia conditions.

D. Impact of $Q - V$ Droop Control

The second-order KBM asymptotic method can also be used to calculate the power angle dynamics considering $Q - V$ droop control. The droop coefficient is generally determined by grid code and its typical value is 0.10 p.u. [42]. To show the impact of droop coefficient, the parameters in Table III is used, and the simulation and calculation results have been shown in Fig. 8. With the increase of droop coefficient K_q from 0 in Case I-A to 0.15 p.u. in Case IV-C, the amplitude of power angle curve decreases, making the power angle at equilibrium position increase. As shown in Fig. 8(a)(d), the

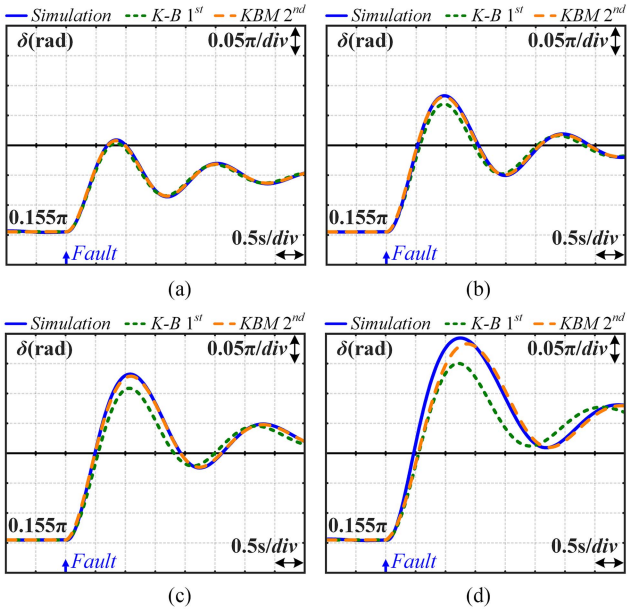

Fig. 5. Simulated and calculated transient responses of GFM control in different fault cases. (a) Case I-A: $k = 0.7(X_{ge2} = 0.78$ p.u.). (b) Case I-B: $k = 0.3(X_{ge2} = 0.86$ p.u.). (c) Case I-C: $k = 0.1(X_{ge2} = 0.94$ p.u.). (d) Case I-D: $k = 0.0(X_{ge2} = 1.00$ p.u.).

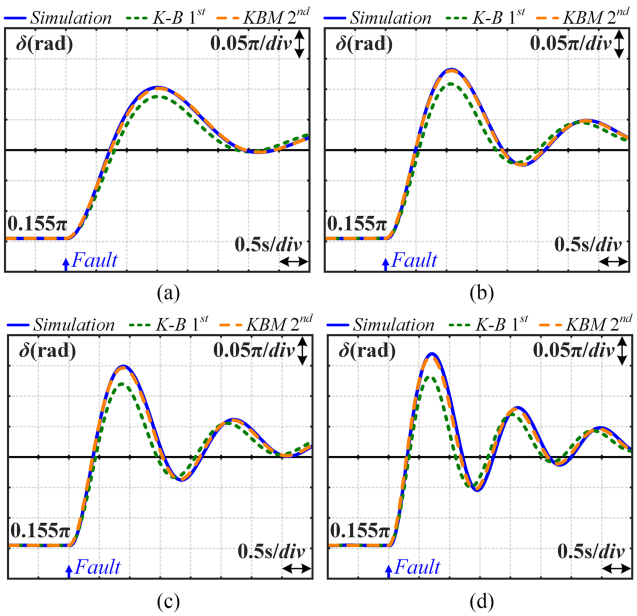

Fig. 6. Simulated and calculated transient responses of GFM control with different droop coefficients. (a) Case II-A: $K_p = 0.02$ p.u. (b) Case I-C: $K_p = 0.04$ p.u. (c) Case II-B: $K_p = 0.06$ p.u. (d) Case II-C: $K_p = 0.10$ p.u.

TABLE III
PARAMETERS FOR SIMULATION AND EXPERIMENTAL TESTS CONSIDERING $Q - V$ DROOP CONTROL

Parameters	K_q	k (X_{ge2})	K_p	ω_p
Case IV-A	0.05 p.u.	0.7 (0.78 p.u.)	0.04 p.u.	0.2·2π rad/s
Case IV-B	0.10 p.u.	0.7 (0.78 p.u.)	0.04 p.u.	0.2·2π rad/s
Case IV-C	0.15 p.u.	0.7 (0.78 p.u.)	0.04 p.u.	0.2·2π rad/s

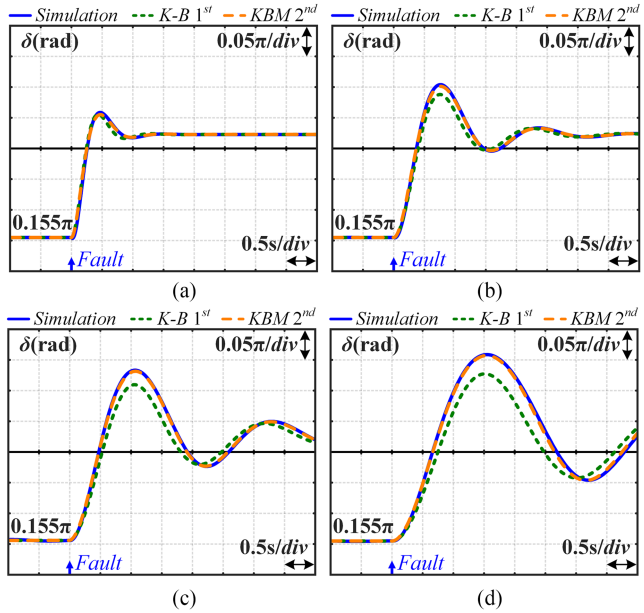

Fig. 7. Simulated and calculated transient responses of GFM control with different cutoff frequencies. (a) Case III-A: $\omega_p = 1.2{\cdot}2\pi$ rad/s. (b) Case III-B:$\omega_p = 0.4{\cdot}2\pi$ rad/s. (c) Case I-C:$\omega_p = 0.2{\cdot}2\pi$ rad/s. (d) Case III-C:$\omega_p = 0.1{\cdot}2\pi$ rad/s.

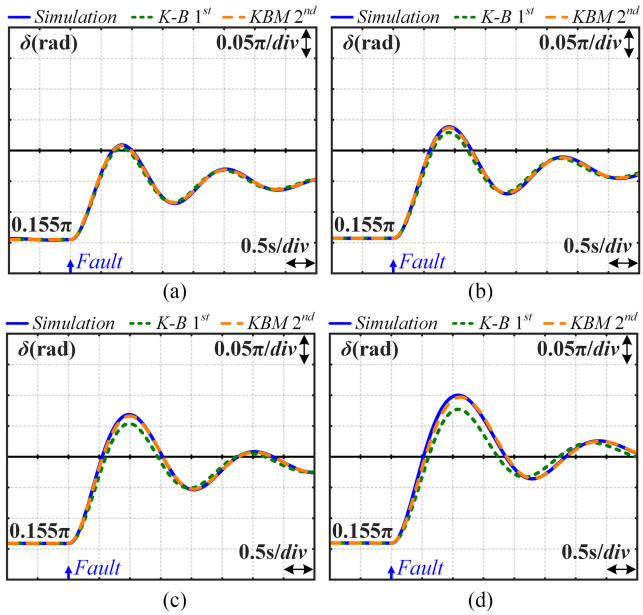

Fig. 8. Simulated and calculated transient responses of GFM control with different $Q - V$ droop coefficients. (a) Case I-A: $K_q = 0$. (b) Case IV-A:$K_q = 0.05$. (c) Case IV-B:$K_q = 0.1$. (d) Case IV-C:$K_q = 0.15$.

equilibrium power angle keeps increasing and the oscillation amplitude increases. In addition, with the increase of K_q, the error of first-order K-B calculation results keeps increasing significantly, while that of the second-order KBM calculation results remains small. In consequence, the effectiveness and advantages of the second-order KBM asymptotic method with $Q - V$ droop control can be validated.

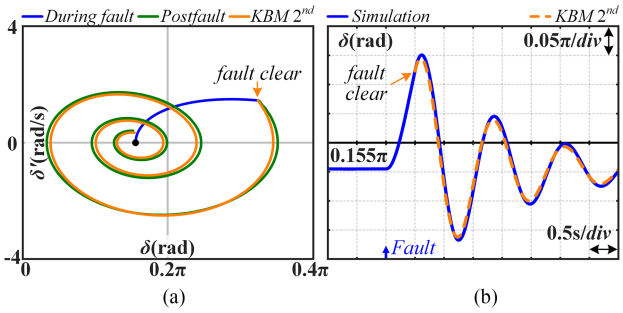

Fig. 9. Simulated and calculated transient responses of GFM control after fault is cleared (a) Phase portrait. (b) Power angle.

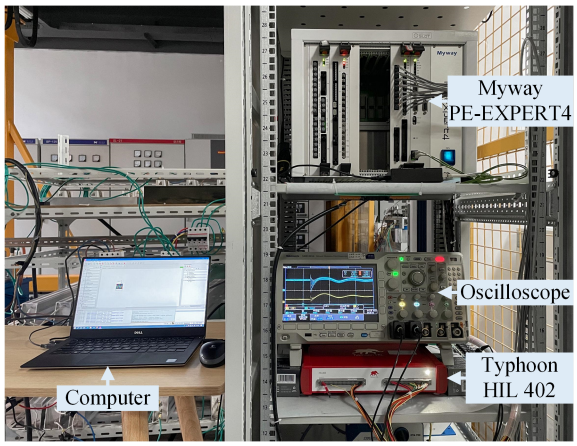

Fig. 10. Control hardware-in-loop experimental platform.

E. Analysis of Postfault Characteristics

In addition to the during-fault characteristics, the proposed method can be also utilized to calculate the postfault power angle dynamics with the initial conditions at the fault clearing time and the postfault parameters. Fig. 9 illustrates the simulated and calculated transient responses of GFM control in the form of both phase trajectories and power angle curve over time. The fault in Case I-D is triggered at $t = 1.0$ s and is cleared at $t = 1.5$ s. The power angle at the time of fault clearing is 1.016 rad and its relative velocity is 1.454 rad/s, which is the initial condition for postfault power angle dynamics calculation. As can be seen from the phase portrait in Fig. 9(a), the velocity δ' decreases and power angle δ growth slows down once the fault is cleared. Moreover, the calculation result of second-order KBM solution in Fig. 9 keeps in line well with the simulation waveform, which validates the effectiveness of the second-order KBM asymptotic method in postfault power angle dynamics calculation of GFM control.

V. Experimental Validation

To further verify the correctness of theoretical analysis and simulation results, experiments have been conducted on the control-hardware-in-loop (CHIL) testing platform shown in Fig. 10 with the same parameters as time-domain simulations. The controller used in the testing is Myway PE-EXPERT4 digital control system, and the power part of the grid-connected system is emulated through Typhoon HIL 402 platform. The power system grounding fault is triggered through Typhoon HIL control center in computer and the experimental waveforms are collected by oscilloscope.

A. Fault Impedance

Fig. 11 illustrates the experimental active power P_e and power angle δ with different fault severities. Four sets of equivalent fault impedance X_{ge2} presented in Case I, varying from 0.78 to 1.0 p.u., are tested. To verify the accuracy of the proposed method under different fault severities, the second-order calculation results of δ are also drawn in the same figure as a comparison. The three-phase grounding fault of transmission line occurs at $t = 1$ s. At the moment of failure, the actual active output power P_e drops abruptly due to the sudden change in grid impedance, and then, gradually returns to the set output power P_0. As the fault becomes more serious, the active power fluctuation becomes larger, leading to greater changes in power angle. Moreover, the impact of power fluctuations on δ is averaged due to the LPF in GFM control. It is clearly shown in the figure that the analytical solutions match well with the experimental results and a small error can be seen only in the case of $k = 0$. The testing results in all cases are in good agreement with the simulations in Fig. 5, which validates the effectiveness of the KBM asymptotic method in various fault impedance conditions again.

B. Droop Coefficient

The experimental responses of the GFM converter and analytical calculation results of δ with different droop coefficients are depicted in Fig. 12. In addition to the base case, three sets of droop coefficients in Case II are tested, and grid fault happens at $t = 1$ s. After fault, the power angle starts to oscillate and its oscillation frequency increases with K_p, but eventually converges to the same equilibrium value due to the same fault equivalent impedance. In the case of $K_p = 0.10$ p.u., there is a slight frequency shift, and in other cases, the second-order calculation results are almost coincident with the experimental waveforms. Therefore, there is no significant difference between experimental results and simulation results. These further verify the correctness of approximate analytical calculation and validity of time-domain simulation verification in Fig. 6.

C. Cutoff Frequency

Fig. 13 illustrates the experimental waveforms of P_e and δ in the case of different cutoff frequencies ω_p when three-phase grounding short circuit occurs. Three more sets of cutoff frequencies in Case III are tested besides the base case (Case I-C), and the analytical results of δ using the second-order KBM asymptotic method are drawn in the corresponding experimental diagrams. With a larger ω_p, the power angle changes more slowly and the time it takes to reach steady state increases. The small visible calculation error only appears at the peak of the waveform

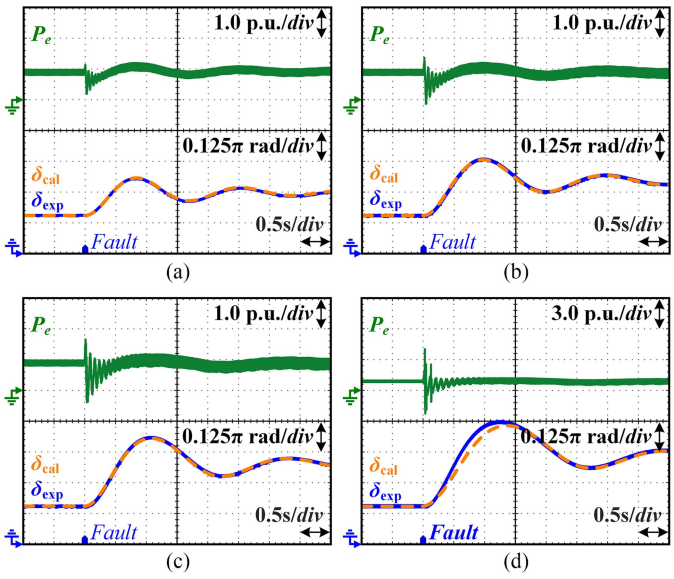

Fig. 11. Experimental transient responses δ(exp) and second-order calculation results δ(cal) of GFM control in different fault cases. (a) Case I-A: $k = 0.7(X_{ge2} = 0.78$ p.u.). (b) Case I-B: $k = 0.3(X_{ge2} = 0.86$ p.u.). (c) Case I-C: $k = 0.1(X_{ge2} = 0.94$ p.u.). (d) Case I-D: $k = 0.0(X_{ge2} = 1.00$ p.u.).

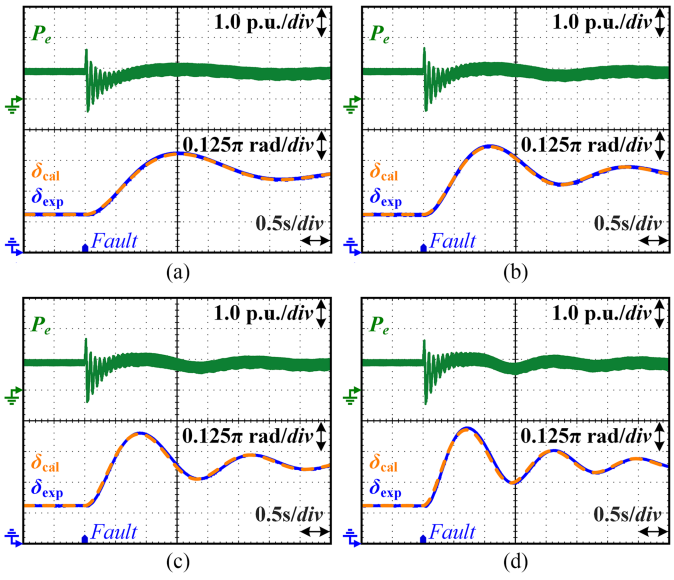

Fig. 12. Experimental transient responses δ(exp) and second-order calculation results δ(cal) of GFM control with different droop coefficients. (a) Case II-A: $K_p = 0.02$ p.u. (b) Case I-C: $K_p = 0.04$ p.u. (c) Case II-B: $K_p = 0.06$ p.u. (d) Case II-C: $K_p = 0.10$ p.u.

in Case III-A as shown in Fig. 13(a), which matches well with the simulation in Fig. 7. In other cases, the differences between the calculated results and experimental results are quite small. These experiments validate the effectiveness of KBM methods under various cutoff frequencies once again.

D. $Q - V$ Droop Control

The experimental response of the GFM converter and second-order calculation results of power angle δ with different $Q - V$

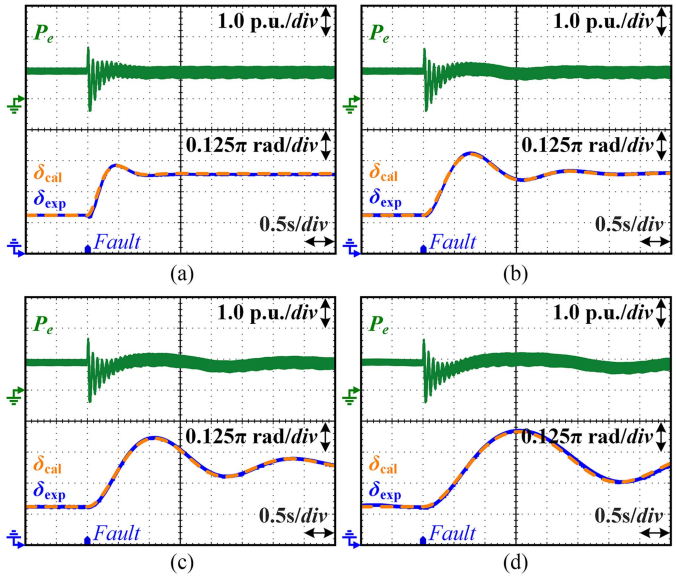

Fig. 13. Experimental transient responses δ(exp) and second-order calculation results δ(cal) of GFM control with different cutoff frequencies. (a) Case III-A: $\omega_p = 1.2{\cdot}2\pi$ rad/s. (b) Case III-B:$\omega_p = 0.4{\cdot}2\pi$ rad/s. (c) Case I-C:$\omega_p = 0.2{\cdot}2\pi$ rad/s. (d) Case III-C:$\omega_p = 0.1{\cdot}2\pi$ rad/s.

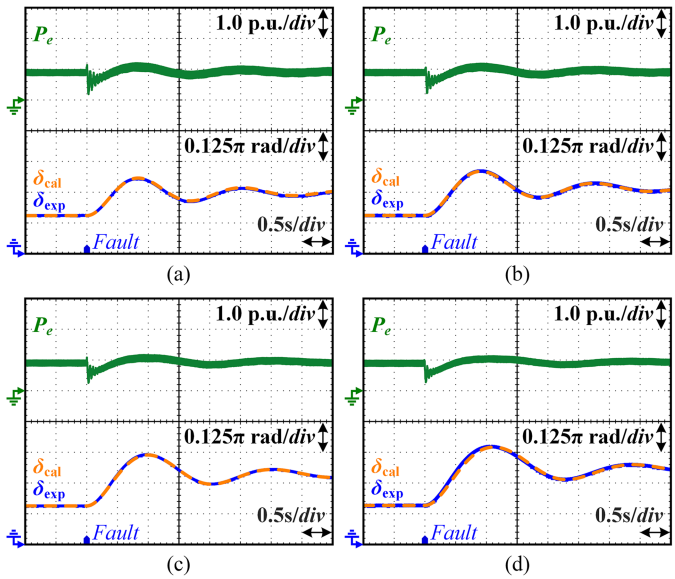

Fig. 14. Experimental transient responses δ(exp) and second-order calculation results δ(cal) of GFM control with different $Q - V$ droop coefficients. (a) Case I-A: $K_q = 0$. (b) Case IV-A:$K_q = 0.05$. (c) Case IV-B:$K_q = 0.10$. (d) Case IV-C:$K_q = 0.15$.

TABLE IV
MATCHING DEGREE OF KBM 2ND SOLUTIONS IN DIFFERENT CASES

Cases	MD_{sim}	MD_{exp}	Cases	MD_{sim}	MD_{exp}
Case I-A	0.9951	0.9903	Case II-B	0.9915	0.9872
Case I-B	0.9941	0.9918	Case II-C	0.9851	0.9791
Case I-C	0.9934	0.9917	Case III-A	0.9881	0.9835
Case I-D	0.9596	0.9546	Case III-B	0.9920	0.9868
Case II-A	0.9927	0.9910	Case III-C	0.9915	0.9841

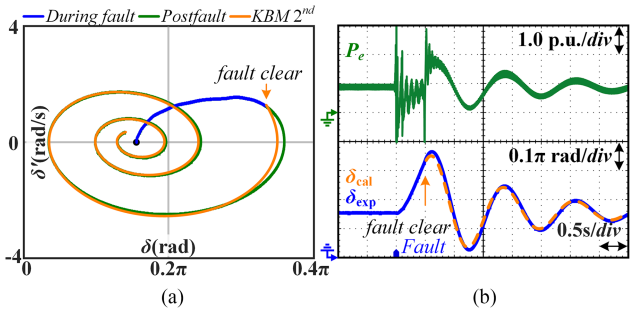

Fig. 15. Experimental and calculated transient responses of GFM control after fault is cleared. (a) Phase portrait. (b) Power angle.

droop coefficients have been illustrated in Fig. 14. Three more sets of droop coefficients varying from 0.05 to 0.15 in Case IV are tested except for the base case (Case I-A). As can be seen from the figure, with the increase of K_q, the equilibrium value and oscillation amplitude of power angle δ_e increase, and the calculated power angle keeps in line with its corresponding experimental waveform, which matches well with the simulation in Fig. 8 and further validate the effectiveness of proposed method when the reactive power control is considered.

E. Postfault Characteristics

Fig. 15 illustrates the experimental and calculated transient responses of GFM control in the form of both phase trajectories and power angle curve over time. The parameters used in experiment are the same as that in simulation, and the fault is also triggered at t=1.0 s and cleared at t=1.5 s. As is can be seen from the experiment waveform, the output active power P_e steps both during the fault occurrence and when the fault is cleared, and it is followed by an adjustment of power angle. The power angle at fault clearing time in experiment is 1.051 rad and the relative velocity is 1.258 rad/s, which is used as the initial condition for postfault power angle calculation. As is shown in the figure, the calculated waveform reach good agreement with the experiment response, which validates the effectiveness of the KBM method in the postfault characteristic calculation again.

F. Matching Degree

To further demonstrate the accuracy of theoretical calculation results quantitatively, the normalized root-mean-square error (NRMSE), a commonly used dataset error evaluation index, is then introduced to measure the similarity between calculation results and simulation or experiment waveforms. It is defined as

$$\mathrm{NRMSE} = \frac{\sqrt{\sum_{i=1}^{N}\left[\delta_{\mathrm{ref}}(i)-\delta_{\mathrm{cal}}(i)\right]^2}}{\sqrt{\sum_{i=1}^{N}\left[\delta_{\mathrm{ref}}(i)\right]^2}} \tag{55}$$

where i and N are the index and total number of sampling point, respectively. Moreover, δ_{ref} and δ_{cal} are the reference waveform and calculation solution of power angle, respectively. The reference waveform δ_{ref} for simulations is δ_{sim} and that for experiments is δ_{exp}. The NRMSE serves to aggregate the magnitude of errors in calculations for various sampling points into a single normalized measure of waveform similarity, which is an average index of curve differences. Its value is always nonnegative and NRMSE=0 indicates a perfect fit of calculated curve to the simulated or experimental waveform. In this article, the total length of waveform is 5 s and 1000 sampling points are used to calculate NRMSE for the sake of accuracy. Based on these, the matching degree (MD) can be further introduced to represent similarity, and it is written as

$$\mathrm{MD} = 1 - \mathrm{NRMSE}. \tag{56}$$

According to its definition, large MD represents high consistency between calculated results using the second-order KBM asymptotic method and simulation waveforms or experimental waveforms. The matching degree for all the aforementioned cases have been calculated and illustrated in Table IV. Subscripts sim and exp are used to distinguish simulation and experimental verification. $\mathrm{MD_{sim}}$ is the matching degree of calculated curve with simulation result and $\mathrm{MD_{exp}}$ is that with experimental waveform. As can be seen in the table, the matching degrees in Case I-D are relatively smaller than others, which is consistent with theoretical analysis in Section IV-A. As for Case III-A, the small error mainly appears at the peak of the waveform and so the match degree after averaging is still high. Moreover, with the decrease of ω_p from Case III-A to Case III-C, both $\mathrm{MD_{sim}}$ and $\mathrm{MD_{exp}}$ increase first due to the weakened loop coupling, and then, decrease due to the increased nonlinearity. In spite of this, $\mathrm{MD_{sim}}$ and $\mathrm{MD_{exp}}$ are quite high in these aforementioned testing cases. These high matching degrees validate the accuracy of calculation results using the KBM asymptotic calculation method quantitatively.

VI. Conclusion

This article introduces a KBM asymptotic method to characterize the power angle trajectory under large disturbances, which provides a new quantitative analysis tool for the GFM converter transient characteristics. On top of that, the angle fluctuation range is taken into consideration, and a tailored integral method, thereby, is further proposed to solve the antiderivative problem and simplify the final calculation results. In this manner, the KBM asymptotic method is effectively adapted to address the complex perturbation function in power angle swing equation of the GFM converter. More importantly, the variation of the GFM converter power angle in the case of large disturbances is clearly characterized using an explicit time-domain expression, and hence, the impact of control and grid parameters can be revealed quantitatively, which shows great potential to be applied to system transient stability analysis and GFM converter design. In the end, the effectiveness and accuracy of the analytical calculations have been verified by both simulation and CHIL experiment, and the theoretical results reach good agreement with simulations and experiments.

Appendix

The explicit expression of U_f and free oscillation frequency ω_o are provided in (57) and (58), shown at the top of the next page, respectively. $P_\Delta(\gamma)$ is the difference between reference

$$U_f(\delta) = \frac{X_1\left(E\cos\delta - X_{ge2}/K_q\right) + \sqrt{X_1^2\left(E\cos\delta - X_{ge2}/K_q\right)^2 + 4X_1X_{ge2}\left(Q_0 + U_0/K_q\right)\left(X_{ge2}+X_1\right)}}{2\left(X_{ge2}+X_1\right)} \tag{57}$$

$$\omega_{oq} = \sqrt{\frac{K_pEU_f(\delta_e)}{X_{ge2}}\cos\delta_e - \frac{K_pE^2U_f(\delta_e)X_1\sin\delta_e^2}{X_{ge2}\sqrt{X_1^2\left(E\cos\delta_e - X_{ge2}/K_q\right)^2 + 4X_1X_{ge2}\left(Q_0+U_0/K_q\right)\left(X_{ge2}+X_1\right)}}}. \tag{58}$$

P_0 and active power P_e, and is shown as follows:

$$P_\Delta(\gamma) = P_0 - \frac{EU_f(\delta_e+\gamma)}{X_{ge2}}\sin(\delta_e+\gamma). \tag{59}$$

REFERENCES

[1] M. G. Taul, X. Wang, P. Davari, and F. Blaabjerg, "An overview of assessment methods for synchronization stability of grid-connected converters under severe symmetrical grid faults," *IEEE Trans. Power Electron.*, vol. 34, no. 10, pp. 9655–9670, Oct. 2019.

[2] J. Lei, Z. Qin, W. Li, P. Bauer, and X. He, "Stability region exploring of shunt active power filters based on output admittance modeling," *IEEE Trans. Ind. Electron.*, vol. 68, no. 12, pp. 11696–11706, Dec. 2021.

[3] J. Zhao, W. Wu, Z. Shuai, A. Luo, H. S.-H. Chung, and F. Blaabjerg, "Robust control parameters design of PBC controller for LCL-filtered grid-tied inverter," *IEEE Trans. Power Electron.*, vol. 35, no. 8, pp. 8102–8115, Aug. 2020.

[4] T. Liu and X. Wang, "Physical insight into hybrid-synchronization-controlled grid-forming inverters under large disturbances," *IEEE Trans. Power Electron.*, vol. 37, no. 10, pp. 11475–11480, Oct. 2022.

[5] Y. Tang, Z. Tian, X. Zha, X. Li, M. Huang, and J. Sun, "An improved equal area criterion for transient stability analysis of converter-based microgrid considering nonlinear damping effect," *IEEE Trans. Power Electron.*, vol. 37, no. 9, pp. 11272–11284, Sep. 2022.

[6] X. He and H. Geng, "Transient stability of power systems integrated with inverter-based generation," *IEEE Trans. Power Syst.*, vol. 36, no. 1, pp. 553–556, Jan. 2021.

[7] X. Fu et al., "Large-signal stability of grid-forming and grid-following controls in voltage source converter: A comparative study," *IEEE Trans. Power Electron.*, vol. 36, no. 7, pp. 7832–7840, Jul. 2021.

[8] R. Rosso, X. Wang, M. Liserre, X. Lu, and S. Engelken, "Grid-forming converters: Control approaches, grid synchronization, and future trends–A review," *IEEE Open J. Ind. Appl.*, vol. 2, pp. 93–109, Apr. 2021.

[9] T. Liu, X. Wang, F. Liu, K. Xin, and Y. Liu, "A current limiting method for single-loop voltage-magnitude controlled grid-forming converters during symmetrical faults," *IEEE Trans. Power Electron.*, vol. 37, no. 4, pp. 4751–4763, Apr. 2022.

[10] L. Huang, H. Xin, Z. Wang, L. Zhang, K. Wu, and J. Hu, "Transient stability analysis and control design of droop-controlled voltage source converters considering current limitation," *IEEE Trans. Smart Grid*, vol. 10, no. 1, pp. 578–591, Jan. 2019.

[11] Z. Jin and X. Wang, "A DQ-frame asymmetrical virtual impedance control for enhancing transient stability of grid-forming inverters," *IEEE Trans. Power Electron.*, vol. 37, no. 4, pp. 4535–4544, Apr. 2022.

[12] C. Shen et al., "Transient stability and current injection design of paralleled current-controlled VSCs and virtual synchronous generators," *IEEE Trans. Smart Grid*, vol. 12, no. 2, pp. 1118–1134, Mar. 2021.

[13] H. Ren et al., "A phase change material integrated press pack power module with enhanced overcurrent capability for grid support on FRD," *IEEE Trans. Ind. Appl.*, vol. 57, no. 4, pp. 3956–3968, Jul. 2021.

[14] W. Shao et al., "A power module for grid inverter with in-built short-circuit fault current capability," *IEEE Trans. Power Electron.*, vol. 35, no. 10, pp. 10567–10579, Oct. 2020.

[15] H. Jiang, J. Wei, X. Fang, H. Ren, W. Shao, and L. Ran, "A $\triangle t_j$ reduced power module with inbuilt phase change material for reliability enhancement," *IEEE Trans. Electron Devices*, vol. 68, no. 9, pp. 4557–4564, Sep. 2021.

[16] J. He, A. Sangwongwanich, Y. Yang, Z. Quan, Y. R. Li, and F. Iannuzzo, "Discontinuous modulation for improved thermal balance of three-level 1500-V photovoltaic inverters under low-voltage ride-through," in *Proc. IEEE Energy Convers. Congr. Expo.*, Vancouver, BC, Canada, 2021, pp. 103–108.

[17] K. Ma and F. Blaabjerg, "Modulation methods for neutral-point-clamped wind power converter achieving loss and thermal redistribution under low-voltage ride-through," *IEEE Trans. Ind. Electron.*, vol. 61, no. 2, pp. 835–845, Feb. 2014.

[18] P. Liu, J. Xu, Y. Yang, H. Wang, and F. Blaabjerg, "Impact of modulation strategies on the reliability and harmonics of impedance-source inverters," *IEEE J. Emerg. Sel. Topics Power Electron.*, vol. 8, no. 4, pp. 3968–3981, Dec. 2020.

[19] Y. Yang, H. Wang, F. Blaabjerg, and T. Kerekes, "A hybrid power control concept for PV inverters with reduced thermal loading," *IEEE Trans. Power Electron.*, vol. 29, no. 12, pp. 6271–6275, Dec. 2014.

[20] M. Andresen, K. Ma, G. Buticchi, J. Falck, F. Blaabjerg, and M. Liserre, "Junction temperature control for more reliable power electronics," *IEEE Trans. Power Electron.*, vol. 33, no. 1, pp. 765–776, Jan. 2018.

[21] Y. Yang, H. Wang, and F. Blaabjerg, "Reactive power injection strategies for single-phase photovoltaic systems considering grid requirements," *IEEE Trans. Ind. Appl.*, vol. 50, no. 6, pp. 4065–4076, Nov./Dec. 2014.

[22] T. Qoria, F. Gruson, F. Colas, G. Denis, T. Prevost, and X. Guillaud, "Critical clearing time determination and enhancement of grid-forming converters embedding virtual impedance as current limitation algorithm," *IEEE J. Emerg. Sel. Topics Power Electron.*, vol. 8, no. 2, pp. 1050–1061, Jun. 2020.

[23] Y. Li, Y. Gu, Y. Zhu, A. Junyent-Ferre, X. Xiang, and T. C. Green, "Impedance circuit model of grid-forming inverter: Visualizing control algorithms as circuit elements," *IEEE Trans. Power Electron.*, vol. 36, no. 3, pp. 3377–3395, Mar. 2021.

[24] C. Yang, L. Huang, H. Xin, and P. Ju, "Placing grid-forming converters to enhance small signal stability of PLL-integrated power systems," *IEEE Trans. Power Syst.*, vol. 36, no. 4, pp. 3563–3573, Jul. 2021.

[25] M. Chen, D. Zhou, and F. Blaabjerg, "Enhanced transient angle stability control of grid-forming converter based on virtual synchronous generator," *IEEE Trans. Ind. Electron.*, pp. 1–1, vol. 69, no. 9, pp. 9133–9144, Sep. 2022.

[26] S. Xia, Z. Ding, M. Shahidehpour, K. W. Chan, S. Bu, and G. Li, "Transient stability-constrained optimal power flow calculation with extremely unstable conditions using energy sensitivity method," *IEEE Trans. Power Syst.*, vol. 36, no. 1, pp. 355–365, Jan. 2021.

[27] M. G. Taul, S. Golestan, X. Wang, P. Davari, and F. Blaabjerg, "Modeling of converter synchronization stability under grid faults: The general case," *IEEE J. Emerg. Sel. Topics Power Electron.*, vol. 10, no. 3, pp. 2790–2804, Jun. 2020.

[28] X. He, S. Pan, and H. Geng, "Transient stability of hybrid power systems dominated by different types of grid-forming devices," *IEEE Trans. Energy Convers.*, vol. 37, no. 2, pp. 868-879, Jun. 2022.

[29] X. He, C. He, S. Pan, H. Geng, and F. Liu, "Synchronization instability of inverter-based generation during asymmetrical grid faults," *IEEE Trans. Power Syst.*, vol. 37, no. 2, pp. 1018–1031, Mar. 2021.

[30] Z. Shuai, C. Shen, X. Liu, Z. Li, and Z. J. Shen, "Transient angle stability of virtual synchronous generators using Lyapunov's direct method," *IEEE Trans. Smart Grid*, vol. 10, no. 4, pp. 4648–4661, Jul. 2019.

[31] H. Cheng, Z. Shuai, C. Shen, X. Liu, Z. Li, and Z. J. Shen, "Transient angle stability of paralleled synchronous and virtual synchronous generators in islanded microgrids," *IEEE Trans. Power Electron.*, vol. 35, no. 8, pp. 8751–8765, Aug. 2020.

[32] H. Wu and X. Wang, "Design-oriented transient stability analysis of grid-connected converters with power synchronization control," *IEEE Trans. Ind. Electron.*, vol. 66, no. 8, pp. 6473–6482, Aug. 2019.

[33] H. Wu and X. Wang, "Design-oriented transient stability analysis of PLL-synchronized voltage source converters," *IEEE Trans. Power Electron.*, vol. 35, no. 4, pp. 3573–3589, Apr. 2020.

[34] T. Liu and X. Wang, "Transient stability of single-loop voltage-magnitude controlled grid-forming converters," *IEEE Trans. Power Electron.*, vol. 36, no. 6, pp. 6158–6162, Jun. 2021.

[35] J. Zhao, M. Huang, H. Yan, C. K. Tse, and X. Zha, "Nonlinear and transient stability analysis of phase-locked loops in grid-connected converters," *IEEE Trans. Power Electron.*, vol. 36, no. 1, pp. 1018–1029, Jan. 2021.
[36] H. Yan, M. Huang, X. Fu, Y. Tang, J. Sheng, and X. Zha, "Transient modeling of phase-locked loop and its applications in a multi-VSCs grid-connected system," in *Proc. IEEE Energy Convers. Congr. Expo.*, Vancouver, BC, Canada, 2021, pp. 858–863.
[37] N. M. Krylov and N. N. Bogoliubov, *Introduction to Nonlinear Mechanics*. Princeton, NJ, USA: Princeton Univ. Press, 1947.
[38] N. N. Bogoliubov and Y. A. Mitropolsky, *Asymptotic Methods in the Theory of Nonlinear Oscillations*. New York, NY, USA: Gordon and Breach, 1961.
[39] Y. A. Mitropolsky, *Problems of the Asymptotic Theory of Nonstationary Vibrations*. New York, NY, USA: Daniel Davey, 1965.
[40] D. Pan, X. Wang, F. Liu, and R. Shi, "Transient stability of voltage-source converters with grid-forming control: A design-oriented study," *IEEE Trans. Emerg. Sel. Topics Power Electron.*, vol. 8, no. 2, pp. 1019–1033, Jun. 2020.
[41] *Standard for Interconnecting Distributed Resources with Electric Power Systems*, IEEE Std. 1547-2003, Jul. 2003.
[42] *Requirements for the Connection of Micro Generators in Parallel With Public Low-Voltage Distribution Networks*, British Std. Inst., BS. EN 50438, 2013.
[43] P. Kundur, *Power System Stability and Control*. New York, NY, USA: McGraw-Hill Education, 1994.

Jintao Lei (Graduate Student Member, IEEE) received the B.S. degree in electrical engineering in 2018 from the College of Electrical Engineering, Zhejiang University, Hangzhou, China, where he is currently working toward the Ph.D. degree in electrical engineering with the College of Electrical Engineering.

His research interests include the modeling and stability analysis of grid-connected power electronic converters.

Xin Xiang (Member, IEEE) received the B.Sc. degree from the Harbin Institute of Technology, Harbin, China, in 2011, the M.Sc. degree from Zhejiang University, Hangzhou, China, in 2014, and the Ph.D. degree from the Imperial College London, London, U.K., in 2018, all in electrical and electronic engineering.

From 2018 to 2020, he was a Research Associate with Imperial College London. He is currently a tenure-track Associate Professor with the College of Electrical Engineering, Zhejiang University. His research interests include the analysis and control of power electronics converters for power system applications.

Dr. Xiang was the recipient of the Eryl Cadwaladr Davies Prize for the Best Ph.D. Thesis of Electrical and Electronic Engineering Department, Imperial College London and the Best Ph.D. Thesis Award from IEEE PELS U.K. and Ireland Chapter.

Wuhua Li (Member, IEEE) received the B.Sc. and Ph.D. degrees in power electronics and electrical engineering from Zhejiang University, Hangzhou, China, in 2002 and 2008, respectively.

From 2004 to 2005, he was a Research Intern, and from 2007 to 2008, a Research Assistant with GE Global Research Center, Shanghai, China. From 2008 to 2010, he joined the College of Electrical Engineering, Zhejiang University as a Postdoctoral. In 2010, he was promoted as an Associate Professor. Since 2013, he has been a Full Professor with Zhejiang University. From 2010 to 2011, he was a Ryerson University Postdoctoral Fellow with the Department of Electrical and Computer Engineering, Ryerson University, Toronto, ON, Canada. He is currently the Executive Deputy Director with the National Specialty Laboratory for Power Electronics and the Vice Director of the Power Electronics Research Institute, Zhejiang University. He has authored and coauthored more than 300 peer-reviewed technical papers and holds more than 50 issued/pending patents. He has excellent teaching and research contributions. His research interests include power devices, converter topologies, and advanced controls for high power energy conversion systems.

Dr. Li was the recipient of the 2012 Delta Young Scholar from Delta Environmental & Educational Foundation, 2012 Outstanding Young Scholar from National Science Foundation of China, 2013 Chief Youth Scientist of National 973 Program, 2014 Young Top-Notch Scholar of National Ten Thousand Talent Program, and 2019 Distinguished Young Scholar from National Science Foundation of China. He serves as the Associate Editor for *Journal of Emerging and Selected Topics in Power Electronics*, *IET Power Electronics*, *CSEE Journal of Power and Energy Systems*, *CPSS Transactions on Power Electronics and Applications*, *Proceedings of the Chinese Society for Electrical Engineering*, a Guest Editor for IET Renewable Power Generation for Special Issue "DC and HVDC system technologies," a Member of Editorial Board for *Journal of Modern Power System and Clean Energy*. He was also the recipient of one National Natural Science Award and four Scientific and Technological Achievement Awards from Zhejiang Provincial Government and the State Educational Ministry of China. He was appointed as the Most Cited Chinese Researchers by Elsevier in 2014.

Xiangning He (Fellow, IEEE) received the B.Sc. and M.Sc. degrees in electrical engineering from the Nanjing University of Aeronautical and Astronautical, Nanjing, China, in 1982 and 1985, respectively, and the Ph.D. degree in electrical engineering from Zhejiang University, Hangzhou, China, in 1989.

From 1985 to 1986, he was an Assistant Engineer with the 608 Institute of Aeronautical Industrial General Company, Zhuzhou, China. From 1989 to 1991, he was a Lecturer with Zhejiang University. In 1991, he obtained a Fellowship from the Royal Society of U.K., and conducted research with the Department of Computing and Electrical Engineering, Heriot-Watt University, Edinburgh, U.K., as a Postdoctoral Research Fellow for two years. In 1994, he joined Zhejiang University as an Associate Professor. Since 1996, he has been a Full Professor with the College of Electrical Engineering, Zhejiang University. He was the Director of the Power Electronics Research Institute, the Head of the Department of Applied Electronics, the Vice Dean of the College of Electrical Engineering, and he is currently the Director of the National Specialty Laboratory for Power Electronics, Zhejiang University. His research interests include power electronics and their industrial applications.

Dr. He was appointed as IEEE Distinguished Lecturer by the IEEE Power Electronics Society during 2011–2015. He is a Fellow of the Institution of Engineering and Technology (formerly IEE), U.K.